Computational analysis of melting radiative heat transfer for solar Riga trough collectors of Jeffrey hybrid-nanofluid flow: A new stochastic approach

Bhupendra K. Sharma [a,*], Anup Kumar [a], Nidhish K. Mishra [b], Ibrahim Albaijan [c], Unai Fernandez-Gamiz [d]

[a] *Department of Mathematics, Birla Institute of Technology and Science, Pilani, Rajasthan, India*
[b] *Department of Basic Science, College of Science and Theoretical Studies Saudi Electronic University, Riyadh, Saudi Arabia*
[c] *Mechanical Engineering Department, College of Engineering at Al Kharj, Prince Sattam Bin Abdulaziz University, Al Kharj 16273, Saudi Arabia*
[d] *Department of Nuclear and Fluid Mechanics, University of the Basque Country (UPV/EHU), Nieves Cano 12, 01006 Vitoria-Gasteiz, Spain*

ARTICLE INFO

ABSTRACT

Current investigation deals with the melting heat transfer for the Jeffrey hybrid-nanofluid flow in parabolic trough solar collectors through Darcy Forchheimer porous media over a variable thick vertical elongation Riga surface under the effect of solar radiation. The impacts of viscous dissipation and Joule heating are also investigated. Equations governing the Jeffrey's hybrid nanofluid flow are higher-order non-linear partial differential equations (PDEs). These governing PDEs are transformed into the non-linear ordinary differential equations (ODEs) by introducing appropriate similarity transformations and dimensionless parameters. Runga Kutta's fourth-order numerical scheme is implemented with the shooting technique to solve coupled higher-order ODEs. Results for velocity profile, temperature profile, drag coefficient and Nusselt number are discussed for various influential parameters. Artificial neural networking is also performed to predict Nusselt numbers in different cases and scenarios. The Artificial Neural Network gives the desired outputs with the highest possible accuracy. It is observed that the temperature profile rises with increase in Hartmann number, porosity parameter, and Forchheimer number. However thermal profile worsens with escalates in the exponential index. Radiant energy of the Sun is a renewable energy source available in considerable amounts in our living environment. A parabolic trough solar collector is an efficient solar collector that stores the concentrated incoming radiant energy from the Sun to fulfill the requirement of high temperatures in thermal energy storage systems. It has various applications in solar-powered appliances for cooking and air conditioning, solar-powered systems for treating wastewater, photovoltaic lighting, solar-powered cars, aircraft, etc.

1. Introduction

The constant rise in energy demand due to high living standards and the increase in population highlights the importance of maximizing solar energy collection. Energy generation using oil, coal, and natural gas has negative environmental consequences. Reducing fossil fuel consumption for energy generation is driving a massive change toward cleaner energy for residential and

commercial use. The parabolic-trough collector concentrates the solar radiation about a fixed axis very efficiently. An absorber tube is placed at the fixed axis or focus of the parabolic trough. The fluid is flowing through the absorber tube, which absorbs the radiant energy from the incoming radiation. Radiant energy stored by the working fluid is usable in various residential and commercial applications. Mu et al. [1] discussed nanofluids' thermal performance and radiative aspects in direct absorption solar collectors. Zhu et al. [2] characterized the ability of nanofluids to absorb solar energy through their thermal radiative features selectively. The absorption of solar radiation using nanofluids containing metallic nano ellipsoids was investigated by Rativa and Gómez-Malagón [3]. A direct absorption solar receiver is developed by Dugaria et al. [4] employing concentrated solar radiation and carbon-based nanofluids. The thermal efficiency and heat transfer in the PTSC by the technique of transient heat flux via TiO_2 nanofluids were examined by Subramani et al. [5]. Malekan et al. [6] studied the heat transfer via Therminol-66/Fe_3O_4 *and* CuO/Therminol- 66 for various types of nanofluids for a PTSC under the impact of applied magnetic field. Mesoporous Silica has been treated with Copper nanoparticles and utilized in a PTSC in the study of Roastami et al. [7]. Jamshed et al. [8] considered the Maxwell-type nanofluid coolant thermal characterization in PTSC for application in solar-powered ships. Jamshed and Nisar [9] also introduced the Keller box method-based Williamson nanofluid single-phase comparative study in a PTSC. Using computational fluid dynamics, the efficiency of a $TiO_2/DI - H_2O$ (De-Ionized Water) nanofluid-filled PTSC with a dimpled tube was evaluated by Arun et al. [10]. Ajbar et al. [11] discussed the thermal performance of a PTSC with various types of hybrid nanofluids.

Saturating porous medium flows has become an essential subject in industry and engineering. Researcher's concentrated on permeable media problems using Darcy's relation, in which the average volume velocity and pressure gradient were directly associated. Darcy's concept was considered in terms of lower velocity and lesser porosity. There are many practical applications in geophysics and energy-related issues, including petroleum resource recovery, geophysical flows, storage of nuclear waste, chemical catalytic reactors, costing solidification, underground electric cables cooling, groundwater pollution, granular insulations and fibers. The value of heat sources in fluid-saturated porous medium are tremendous in these contexts. Sopian et al. [12] examined thermal performance without and with porous media in double-pass collector. Solar radiation-induced boundary-layer natural convection flow of varying porosity immersed in the porous medium over flat plate was described by Chamkha et al. [13]. Modeling of heat transfer through porous media for solar collector by CFD (computational fluid dynamics) techniques was done by Gómez et al. [14]. Sharma et al. [15] described the heat-induced in flow of pulsatile magneto blood in the porous media. A microchannel with permeable plates and electrically conducting viscous nanofluid flow was used to study the heat transfer by Ibáñez et al. [16]. Natural convection in nanofluid flowing through Darcy-Forchheimer porous medium with the impact of solar radiation along the flat sheet was explained by Chakraborty et al. [17]. Thermal aspects of heat transfer in a curved porous artery with stenosis on MHD blood flow was studied by Tripathi and Sharma [18]. Sharma et al. [19] investigated the unsteady fluid flow across an inclined stretched sheet in a porous material. The MHD blood flow in two-phase with varying viscosity in permeable curved artery for analyzing the heat transfer was addressed by Kumawat et al. [20]. The influence of Joule heating in a Darcy-Forchheimer porous media on a vertically elongated surface was analyzed by Gandhi and Sharma [21].

The Riga plate creates wall-parallel Lorentz forces as explained by Pantokratoras and Magyari [22]. The flow characteristics over Riga plates are crucial to numerous engineering and industrial applications. These techniques involve designing liquid metal systems of cooling, MHD generators, nuclear reactors, in meters of blood flow, pumps, etc. Moreover, it is utilized in thermal reactors to regulate the neutron rate of diffusion. Researchers have yet to extensively study the properties of fluid flows caused by the Riga surface. Farooq et al. [23] discussed the melting transfer of heat with the heterogeneous reactions and homogeneous reactions in a viscous fluid flow past a variably thicked Riga surface. Heat transfer along the thicked nonlinear Riga plate with thermally stratifies viscous fluid was addressed by Anjum et al. [24]. Ragupathi et al. [25] investigated the heat transfer under the impact of Fe_3O_4 and Al_2O_3 nanoparticles in different fluids flow past a Riga plate. The heat transfer due to nanofluid flow through two elongation rotating discs examined by Hosseinzadeh et al. [26] under the influence of magnetohydrodynamic (MHD) and solar radiation. The effects of radiation on mixed convective micropolar nanofluid flow of titanium alloy over Riga plate was described by Zaib et al. [27]. Shoaib et al. [28] developed an artificial neural network for a magnetohydrodynamic nanofluid flow for investigating the heat transfer under the effect of solar radiation between two rotating discs. Sharma et al. [29] examined the influences of exponential and thermally dependent heat sources on the EMHD flow of Jeffrey fluid over a vertically extending surface. Salawu et al. [30] did hybrid nanofluid flow in the electromagnetic actuator's thermal convection and solar radiation to enhance solar collector performance. The heat transfer in the mixed convective MHD flow past an elongating surface was introduced by Sharma et al. [31]. Gandhi et al. [32] introduced the CuO and Al_2O_3 nanoparticle-containing non-Newtonian flow of blood with porous walls in diseased artery with irregular stenosis. The EMHD Jeffrey fluid flow in terms of viscous dissipation and Ohmic heating past a non-linear variably thicked vertical elongating surface was explored by Sharma et al. [33]. Micro polar fluids with MHD effects induced by a permeable stretched sheet was studied by Sharma et al. [34].

The efficiency of solar collector is greatly affected by their working fluid. The hybrid nanofluids exhibits significantly higher efficiencies than conventional fluids because of the enhanced thermohysical features of the nanoparticles. Abbas et al. [35] investigated the flow of a hybrid micropolar nanofluid under slip conditions through the Riga channel. Sudarsana and Sreedevi [36] did the investigation of heat transfer due to thermal radiation for the MHD hybrid nanofluid's flow inside a square cavity. Tiwari et al. [37] described the utilization and applications of hybrid nanofluids in PTSCs. A study of hybrid viscoelastic nanofluid flow for the applications of the solar-powered ship using the Galerkin finite element approach was done by the Bayones et al. [38]. Sharma et al. [39] investigated the entropy formation in thermally radiated hybrid nanofluids with MHD slip flow via a stenosed artery with tapered walls. Saranya et al. [40] explored the free convection hybrid ferrofluid flow by a rotating heated cone. Gandhi et al. [41] studied MHD blood flow in permeable-walled artery for the heat transfer in an irregular stenosis of various-shaped hybrid nanoparticles. The radiation effect-driven axisymmetric EMHD hybrid nanofluid's flow over a Riga surface was studied by Khashi'ie

et al. [42]. Salah et al. [43] analyzed the impact of heating conditions on a rotating cone-shaped with ternary hybrid $Al + Mg + TiO_2$ water-ethylene glycol nanofluid. Saranya et al. [44] studied the heterogeneous-homogeneous quadratic processes in a hybrid ternary-nanofluid of water with titanium, copper and alumina nanoparticles. Considered hybrid Nanofluids are formulated by dispersing both Copper (Cu) nanoparticles and Multiwalled Carbon Nanotubes (MWCNTs) in a solution of poly-vinyl alcohol/water. The article by Shahzad et al. [45] analyzed the heat transfer by the composition of different nanoparticles and base fluids. It is concluded that copper nanoparticles in poly-vinyl alcohol/water base fluid work as the best heat transfer nanofluid as compare to other nanofluids. Kumar et al. [46] also implemented the response surface methodology for sensitivity analysis of heat transfer in Jeffrey nanofluid flow with poly-vinyl alcohol/water base fluid. Moreover, multiwalled carbon nanotubes are superior due to low cost, ease of mass manufacture, simple functionalization, and improved stabilities. Hybrid nanofluids have various industrial applications, including solar thermal collectors, photovoltaic cooling systems, radiators and heat exchangers, automotive and aerospace cooling systems, nuclear reactor cooling, and biomedical applications like hyperthermia treatments. Investigating the melting heat transfer especially using hybrid-nanofluid flows in parabolic trough solar collectors, can integrate the harnessing of renewable solar energy sources. This multifaceted research endeavors the potential to boost the sustainability, efficiency, and viability of solar thermal systems. The hybrid nanofluids provides better heat transfer characteristics and are cutting-edge fluids engineered by the suspension of two or more types of nanoparticles in the traditional heat transfer fluids. Investigating their behavior within parabolic trough collectors can significantly augment heat absorption, retention, and distribution, ultimately translating to heightened overall system performance. Therefore, a combination of Copper (Cu) and multiwalled carbon nanotubes (MWCNT) hybrid nanoparticles is taken in the current investigation to analyze heat transfer in Jeffrey hybrid nanofluid (Cu *and* MWCNT-PVA/water) flow over a variably thicked Riga surface through Darcy-Forchheimer porous media. The Jeffrey model is a simplified non-Newtonian fluid model which employs temporal derivatives rather than computed ones like in the Maxwell model by Zainal et al. [47].

Novelty of the present model is as follows:

- Radiative heat transfer for the Jeffrey hybrid nanofluid flow through parabolic trough solar collectors over elongating Riga surface is analyzed.
- The influences of Ohmic heating, viscous dissipation, and Darcy Forchheimer porous media are investigated.
- Copper (Cu) and multiwalled carbon nanotubes (MWCNT) are used as the hybrid nanoparticles in polyvinyl-alcohol/water-based fluid.
- The performance of Artificial Neural Networking is analyzed to predict the Nusselt number for various cases and scenarios.

2. Model formulation

Formulation of the fluid model is done in the terms of the assumption of fluid model, defining governing equation for the assumption of the Jeffrey hybrid nanofluid flow, introducing similarity variables and dimensionless parameters to the equations governing the Jeffrey hybrid nanofluid flow, and the application of the numerical technique to the non-dimensionalized governing ordinary differential equations. All these steps for the formulation of the fluid model are described below:

2.1. Assumptions of the problem

In this study, A 2-dimensional laminar steady flow is considered to analyze the melting heat transfer under the effect of viscous dissipation, Darcy Forchheimer porous medium, and solar radiation over variably thicked vertically elongating Riga surface. Vertical and horizontal directions are along the *x*-axis and *y*-axis, and their velocity components are *u* and *v*. The magnetic field induced in the hybrid nanofluid is disregarded by the assumptions of low Reynolds number. The vector product $F_0 = J_0 \times B_0$, determines the volume density of the Lorentz force, where J_0 is the fluid's induced electric current density and B_0 is its magnetic field. Ohm's law determines the current density: $J_0 = \sigma_0(E_0 + V_0 \times B_0)$, where E_0 is the electric field and V_0 is fluid velocity. Fluids with strong electrical conductivity, 10^6 S/m, can be controlled contactless without electric fields. The Lorentz force is $F_0 = J_0 \times B_0 \approx \sigma_0(V_0 \times B_0)B_0$, and moderately 1 T of applied magnetic fields is enough to establish MHD flow control. The current density $\sigma_0(V_0 \times B_0)$ produced by magnetic fields of many Tesla is insufficient and negligible in fluids with low electrical conductivities of less than 10 S/m. Hence, an external electric field is needed to govern low-electrical conductivity fluid flows. With low-electrical conductivity fluid flows, the Lorentz force is independent of $F_0 = J_0 \times B_0 \approx \sigma_0(E_0 \times B_0)$.

The Riga plate's applied electric and magnetic fields only have spanwise *Z* and wall-normal *Y* components, neglecting edge effects. Hence, the Lorentz force, $F_0 = (E_0 \times B_0)$, points x-ward. The stripwise plate causes considerable spanwise changes in F close to its surface, but these variations gradually reduce as *Y* increases. Along the spanwise coordinate *Z*, the average density of force is a function exponentially decreasing in the direction *Y*:

$$F_0 = \frac{\pi J_0 M}{8\tilde{\rho}} exp\left(-\frac{\pi}{\tilde{b}} y\right)$$

where $\tilde{b}$ is the permanent magnet and electrode width, *M* (Tesla) is the magnetization, and J_0 (A/m^2) is the electrode current density. Pictorial representation of the fluid model is shown in the Fig. 1

Components of stress tensor in model of Jeffrey fluid are written as:
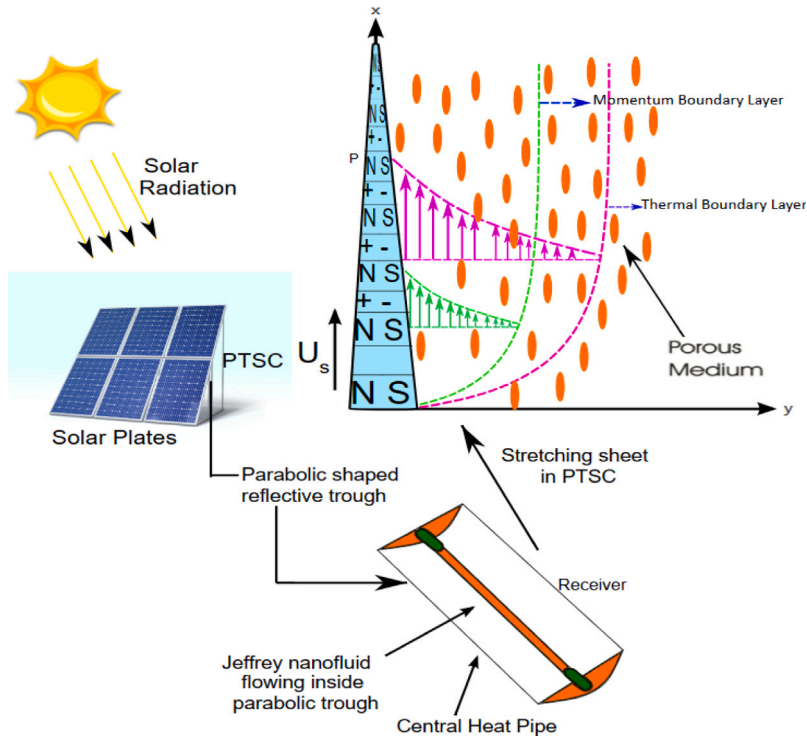
$$T = -PI + S, \tag{2.1}$$

Fig. 1. Pictorial representation of the problem.

where S is mathematically termed as:

$$\mathbf{S} = \frac{\mu_{hnf}}{1 + \lambda_1}\left[\mathbf{A} + \lambda_2\frac{d\mathbf{A}}{dt}\right], \tag{2.2}$$

where, the Rivlin Erection tensor A of first-order is written as

$$\mathbf{A} = \nabla V + (\nabla V)',$$

where $'$ denotes the transpose.

2.2. Equations governing the boundary layer flow

Equations governing the boundary layer flow for a two-dimensional, incompressible Jeffrey hybrid nanofluid are [33,48]:

$$\frac{\partial u}{\partial x} + \frac{\partial v}{\partial y} = 0, \tag{2.3}$$

$$
\begin{aligned}
u\frac{\partial u}{\partial x} + v\frac{\partial u}{\partial y} &= \frac{v_{hnf}}{(1+\lambda_1)}\left[\frac{\partial^2 u}{\partial y^2} + \lambda_2\left(u\frac{\partial^3 u}{\partial x\partial y^2} + \frac{\partial u}{\partial y}\frac{\partial^2 u}{\partial x\partial y} + v\frac{\partial^3 u}{\partial y^3} + \frac{\partial v}{\partial y}\frac{\partial^2 u}{\partial y^2}\right)\right] + \frac{\pi J_0 M}{8\rho_{hnf}}exp\left(-\frac{\pi}{\bar{b}}y\right) - \frac{v_{hnf}}{K_1}u \\
&\quad - \frac{c_b}{\sqrt{K_1}}u^2 + g(\beta_T)_{hnf}(T - T_l),
\end{aligned}
\tag{2.4}
$$

$$
\begin{aligned}
u\frac{\partial T}{\partial x} + v\frac{\partial T}{\partial y} &= \frac{k_{hnf}}{(\rho Cp)_{hnf}}\frac{\partial^2 T}{\partial y^2} + \frac{16\sigma_e T_l^3}{3k^*(\rho c_p)_{hnf}}\frac{\partial^2 T}{\partial y^2} + \frac{\mu_{hnf}}{(\rho Cp)_{hnf}(1+\lambda_1)}\left[\left(\frac{\partial u}{\partial y}\right)^2 + \lambda_2\left(u\frac{\partial u}{\partial y}\frac{\partial^2 u}{\partial x\partial y} + v\frac{\partial u}{\partial y}\frac{\partial^2 u}{\partial y^2}\right)\right] \\
&\quad \frac{\pi J_0 M}{8(\rho c_p)_{hnf}}exp\left(-\frac{\pi}{\bar{b}}y\right)u.
\end{aligned}
\tag{2.5}
$$

$$u = U_s(x), \quad v = 0, \quad T = T_s, \quad at \quad y = A(x+b)^{\frac{1-n}{2}},$$

$$u \to 0, \quad T \to T_l, \quad as \quad y \to l. \tag{2.6}$$

Table 1

Physical properties of the hybrid nanofluid.

Physical properties	Copper	MWCNT	PVA	Water
Coefficient of thermal expansion $[\beta_T \times 10^{-5} \, (\text{K}^{-1})]$	1.67	44	2.5	21
Thermal conductivity $[\kappa \, (\text{W/m K})]$	401	3000	0.2	0.613
Heat capacitance $[C_p \, (\text{J/kg K})]$	385	796	2000	4179
Density $[\rho \, (\text{kg/m}^3)]$	8933	1600	1020	997

Table 2

Non-dimensionalized parameters.

$$\epsilon_3 = (1-\phi_2)(1-\phi_1+\phi_1 \frac{\rho c_{p_1}}{\rho_f c_{p_f}}) + \phi_2 \left(\frac{\rho c_{p_2}}{\rho c_{p_f}} \right) \qquad \epsilon_2 = (1-\phi_2)(1-\phi_1+\phi_1 \frac{\rho_1}{\rho_f}) + \phi_2 \frac{\rho_2}{\rho_f} \qquad Pr = \frac{\mu C_p}{\kappa}$$

$$\epsilon_4 = (1-\phi_2)(1-\phi_1+\phi_1 \frac{\beta_{T_1}}{\beta_{T_f}}) + \phi_2 \frac{\beta_{T_2}}{\beta_{T_f}} \qquad Nr = \frac{16\sigma T_l^3}{3\kappa_f \kappa^*} \qquad a_1 = \frac{\pi}{b} \sqrt{\frac{2}{(n+1)} \frac{v_f(x+b)}{U_s}}$$

$$\epsilon_6 = \frac{k_{hnf}}{k_f} \qquad M_0 = \frac{\pi J_0 M}{8\rho_f U_s^2} \frac{2(x+b)}{n+1} \qquad K_p = \frac{2(x+b)v_f}{K_1 U_s(n+1)}$$

$$\alpha = A\sqrt{\frac{a(n+1)}{2v}} \qquad Fr = \frac{2c_b(x+b)}{\sqrt{K_1}(n+1)} \qquad Ec = \frac{U_s^2}{C_p(T_s-T_l)},$$

$$\epsilon_1 = \frac{1}{(1-\phi_1)^{2.5}(1-\phi_2)^{2.5}} \qquad Gr = \frac{2g\beta_T(T_s-T_l)(x+b)}{U_s^2}$$

$$k_{hnf}(\frac{\partial T}{\partial y}) = \rho_f[\lambda + c_s(T_m - T_l)]v(x,0)$$

where k^* is the coefficient of absorption, σ_e is the Stefan–Boltzmann constant, n is the power index and $U_s(x) = a(x+b)^n$, is the stretching surface velocity at $y = A(x+b)^{\frac{(1-n)}{2}}$. Physical properties of the hybrid nanoparticles and fluid are given in Table 1:

Expressions used for evaluating the effective physical properties of hybrid nanofluids:

Dynamic viscosity

$$\mu_{hnf} = \frac{\mu_f}{\left(1-\phi_1\right)^{2.5}\left(1-\phi_2\right)^{2.5}},$$

Density

$$\rho_{hnf} = \left(1-\phi_1\right)\left[\left(1-\phi_2\right)\rho_f + \phi_2\rho_2\right] + \phi_1\rho_1,$$

Coefficient of thermal expansion

$$\beta_{T\,hnf} = \left(1-\phi_1\right)\left[\left(1-\phi_2\right)\beta_{Tf} + \phi_2\beta_{T2}\right] + \phi_1\beta_{T1},$$

Specific heat capacity

$$\left(\rho c_p\right)_{hnf} = \left(1-\phi_1\right)\left[\left(1-\phi_2\right)\left(\rho c_p\right)_f + \phi_2\left(\rho c_p\right)_2\right] + \phi_1\left(\rho c_p\right)_1,$$

Thermal conductivity

$$k_{hnf} = \frac{k_1 + 2k_{nf} - 2\phi_1\left(k_{nf}-k_1\right)}{k_1 + 2k_{nf} + \phi_1\left(k_{nf}-k_1\right)} \times \left(k_{nf}\right),$$

where

$$k_{nf} = \frac{k_2 + 2k_f - 2\phi_2\left(k_f-k_2\right)}{k_2 + 2k_f + \phi_2\left(k_f-k_2\right)} \times \left(k_f\right),$$

2.3. Similarity variables

Most accurate fluid mechanics solutions are similarity solutions with independent variables. Similarity results are utilized as asymptotic situation results to understand complex fluid flows physically. These solutions show the physical, dynamic, and thermal characteristics and their effects. The similarity variables to obtain the dimensionless governing equations are given:

$$u = \frac{\partial \psi}{\partial y} = U_s(x)F'(\zeta), \quad v = -\frac{\partial \psi}{\partial x} = -\sqrt{\frac{(n+1)va}{2}}(x+b)^{\frac{n-1}{2}}\left(F(\zeta) + \eta\frac{n-1}{n+1}F'(\zeta)\right), \quad \theta = \frac{T-T_l}{T_s-T_l},$$

$$\zeta = y\sqrt{\frac{n+1}{2}\frac{a}{v}}(x+b)^{\frac{n-1}{2}}, \quad \psi = F(\zeta)\sqrt{\frac{2}{n+1}va}(x+b)^{\frac{n+1}{2}}. \tag{2.7}$$

Non-dimensionalized parameters involved in the study are written in Table 2:

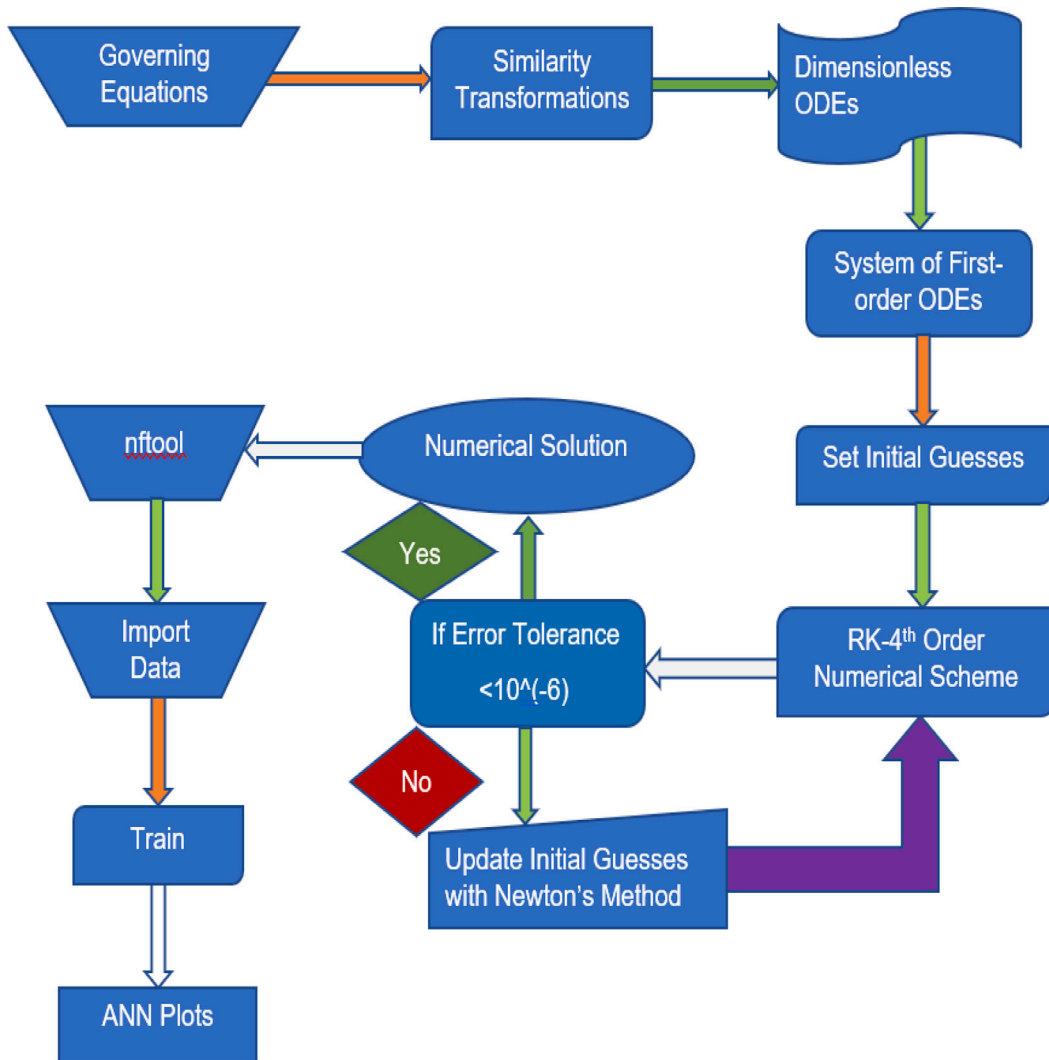The following governing equations are obtained after applying the similarity variables:

$$F'''(\zeta) + (1 + \beta_1)\frac{\varepsilon_2}{\varepsilon_1}[F''(\zeta)F(\zeta) - \frac{2n}{n+1}F'^2(\zeta)] + (1 + \beta_1)\frac{\varepsilon_4}{\varepsilon_1}[\varepsilon_2 Gr\theta(\zeta) - \varepsilon_1 K_p F'(\zeta) - FrF'' + M_0\exp(-a_1\zeta)]$$

$$+ \beta_2\left[\frac{3n-1}{2}(F''(\zeta))^2 + (n-1)F'(\zeta)F'''(\zeta) - \frac{n+1}{2}F(\zeta)F^{iv}(\zeta)\right] = 0, \tag{2.8}$$

$$\theta''(\zeta) + \frac{\varepsilon_3}{(\varepsilon_6 + Nr)}Pr[F(\zeta)\theta'(\zeta)] + \frac{1}{(\varepsilon_6 + Nr)}Pr[M_0 Ec\exp(-a_1\zeta)F'(\zeta)] + \frac{PrEc\varepsilon_1}{(1+\beta_1)(\varepsilon_6 + Nr)}\left[F''^2(\zeta)\right]$$

$$+ \beta_2\left(\frac{3n-1}{2}F'(\zeta)(F''(\zeta))^2 - \left(\frac{n+1}{2}\right)F(\zeta)F''(\zeta)F'''(\zeta)\right)\right] = 0, \tag{2.9}$$

Boundary conditions in non-dimensionalized form:

$$Me\theta'(\zeta) + Pr\left(F(\zeta) - \alpha\left(\frac{1-n}{1+n}\right)\right) = 0, \quad F'(\zeta) = 1, \quad \theta(\zeta) = 1, \quad \text{at } \zeta = 0, \tag{2.10}$$

$$F'(\zeta) \to 0, \quad \theta(\zeta) \to 0, \quad \text{as } \zeta \to l. \tag{2.11}$$

2.4. Numerical procedure

The non-dimensionalized governing equations are higher-order non-linear coupled ODEs. Resulting higher-order, coupled non-linear ODEs are solved using a numerical approach by reducing them to a set of first-order ODEs with appropriate boundary conditions. The system of ODEs is than solved using the shooting technique with the explicit Runga Kutta fourth-order numerical scheme. Four initial conditions are required for solving the momentum equation, two initial conditions are required for solving the energy equation to apply the Runga Kutta fourth-order approach. However, the energy equation has only one initial condition, while the momentum equation has two. The remaining ones are therefore obtained by utilizing Newton's method to update the initial predictions. Flowchart of the numerical procedure is shown in Fig. 2.

$$\begin{cases} F = F, \quad F' = F_1, \quad F'' = F_2, \quad F''' = F_3, \\ \theta = F_4, \quad \theta' = F_5, \quad \theta'' = F_6, \end{cases} \tag{2.12}$$

The differential equations in the first-order system:

$$\begin{cases} F' = F_1, \\ F'_1 = F_2, \\ F'_2 = F_3, \\ F'_3 = \frac{2F_3}{(n+1)\beta_2 F} + \frac{2(1+\beta_1)\varepsilon_2}{\beta_2(n+1)F\varepsilon_1}[FF_2 - \frac{2n}{n+1}F_1^2] + \frac{2\varepsilon_4(1+\beta_1)}{\varepsilon_1\beta_2(n+1)F}[\varepsilon_2 GrF_4 - \varepsilon_1 K_p F_2 - FrF_2^2 + M_0\exp(-a_1\zeta)] \\ \qquad\qquad\qquad\qquad\qquad + \frac{2}{(n+1)F}\left[\left(\frac{3n-1}{2}\right)(F_2)^2 + (n-1)F_1 F_3\right] \\ F'_4 = F_5, \\ F'_5 = F_6 = -\frac{\varepsilon_3 Pr}{(\varepsilon_6 + Nr)}[FF_5] + \frac{1}{(\varepsilon_6 + Nr)}Pr[M_0 Ec\exp(-a_1\zeta)F_1] + \frac{PrEc\varepsilon_1}{(1+\beta_1)(\varepsilon_6 + Nr)}\left[F_2^2 + \beta_2\left(\frac{3n-1}{2}FF_2^2 - \frac{n+1}{2}FF_2 F_3\right)\right] \end{cases} \tag{2.13}$$

and the boundary conditions becomes:

$$\begin{cases} MeF_5(\zeta) + Pr\left(F(\zeta) - \alpha\left(\frac{1-n}{1+n}\right)\right) = 0, \quad F_1(\zeta) = 1, \quad F_4(\zeta) = 1, \quad \text{at } \zeta = 0, \\ F_1(\zeta) \to 0, \quad F_4(\zeta) \to 0, \quad \text{as } \zeta \to l. \end{cases} \tag{2.14}$$

3. Analysis of graphical results

This study investigates the melting heat transfer in hybrid Jeffrey nanofluid flow due to solar radiation under the impacts of Darcy Forchheimer porous media and viscous dissipation over variably thicked vertically elongating Riga surface. The governing equations are coupled with higher-order PDEs converted into ODEs by introducing appropriate similarity variables and dimensionless parameters. The resulting higher-order ODEs are then solved with Runga Kutta's fourth-order numerical scheme in conjunction with the iterative shooting technique. The obtained numerical solution is validated with the previously published article by Sharma et al. [33]. To validate the outcomes of the investigation, the influences of extra parameters of the study [33] like Nt, Nb, Lb, E_1, M, Pe, δ_N, and K and additional parameters of the present study like M_0, a_1, K_p, Me, Fr, and ϕ_2 are taken as zero. And the remaining common parameters are set to their default values to validate the current analysis with the existing one. The validation

Fig. 2. Graphical abstract of the numerical procedure.

plots for the fluid velocity and temperature results are shown in Figs. 3(a) and 3(b). These Figures reveal that the numerical outputs of the study are in excellent agreement with validation. Default values taken in the study are $Pr = 7.743$, $\beta_1 = 0.5$, $\beta_2 = 0.5$, $Ec = 0.5$, $n = 0.5$, $Gr = 0.5$, $M_0 = 0.5$, $a_1 = 1$, $K_p = 0.5$, $Fr = 0.5$, $Nr = 1$, $Me = 0.5$, $\phi_1 = \phi_2 = 0.03$.

3.1. Fluid velocity results

Fig. 4 shows the fluid velocity results due to various important physical parameters. Fig. 4(a) presents the dimensionless velocity profiles $f'(\zeta)$ affected by varying the modified Hartmann number (M_0). From this Figure, it is examined that the improvement in modified Hartmann number M_0 is gradually increased from 0 to 1.5, the velocity profile $f'(\zeta)$ demonstrates a significant enhancement along with enhancement in the thickness of the momentum boundary layer. Physically, the growing values of the Hartmann number correspond to the higher external electric field. Therefore, the larger electric field accelerates the fluid flow, and hence velocity profile escalates. The effect of exponential index parameter (a_1) on the fluid velocity is illustrated in Fig. 4(b), which declares that increasing a_1 diminishes the velocity profile. Because the higher values of a_1 weaken the strength of electromagnetic forces produced by the Riga plate, which slows down the velocity profile. Figs. 4(c) and 4(d) represent the influence of the porosity parameter (k_p) and Forchheimer number (Fr) on the velocity profile. These Figures illustrates that the velocity profile is reduced with escalates in the Forchheimer number and porosity parameter. The porosity indicates that the permeability is too low; fluid flow is not feasible for a medium with low permeability. Because the porosity of the medium opposes the hybrid nanofluid flow, the effect of porosity opposes fluid flow and generates growing flow retardation; therefore, fluid velocity decreases. The relationship between the melting temperature parameter and the fluid velocity is demonstrated in Fig. 4(e). As per this Figure, the velocity

(a) Validation plot for $F'(\zeta)$

(b) Validation plot for $\theta(\zeta)$
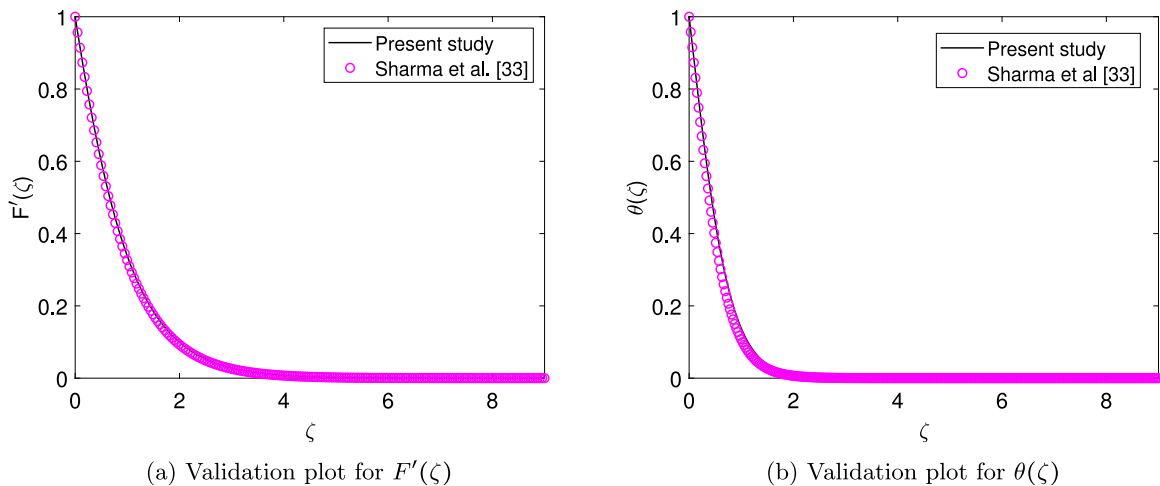
Fig. 3. Validation of the velocity profile 3(a) and temperature profile 3(b) with study of Sharma et al. [32].

(a) Behavior of $F'(\zeta)$ via M_0

(b) Behavior of $F'(\zeta)$ via a_1

(c) Behavior of $F'(\zeta)$ via k_p

(d) Variation in $F'(\zeta)$ via Fr

(e) Variation in $F'(\zeta)$ via Me

(f) Variation in $F'(\zeta)$ via Nr
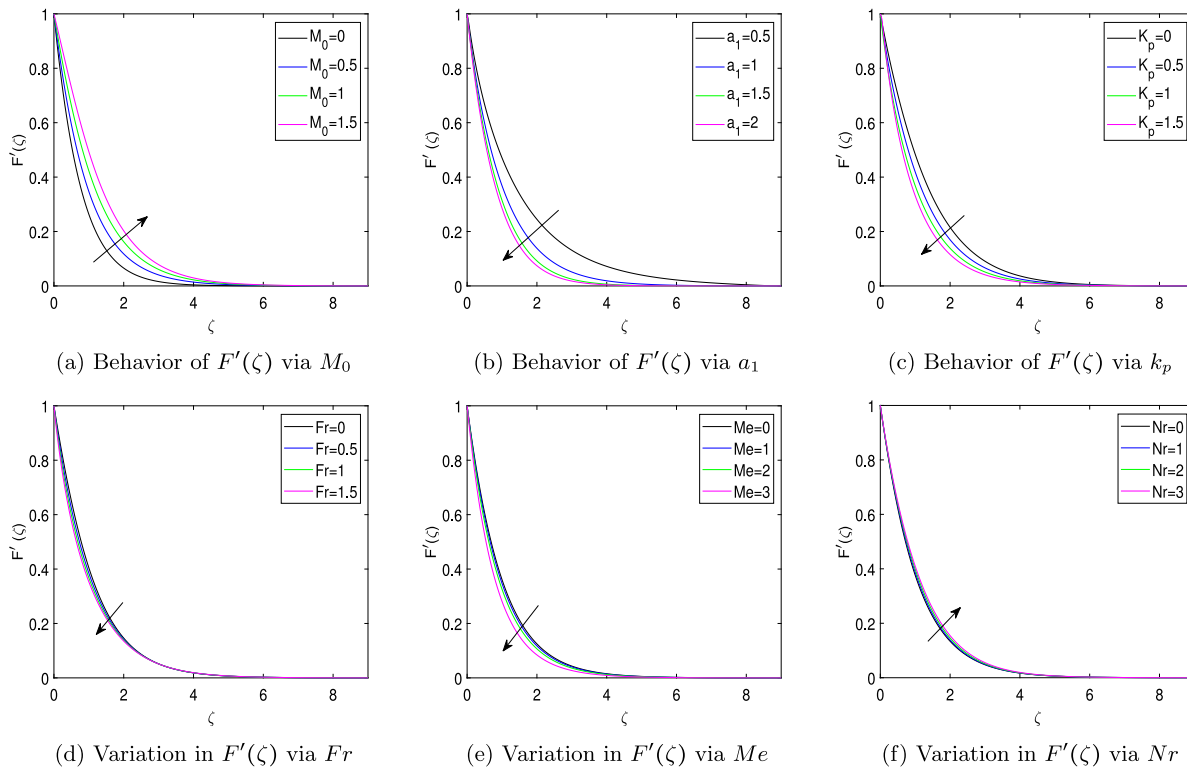
Fig. 4. Plots of the fluid velocity against numerous influential physical parameters.

profile decelerates with an increase in melting heat parameter. Fig. 4(f) reveals the effect of the thermal radiation parameter (Nr) on fluid velocity. This Figure shows that the higher values of the thermal radiation parameter escalate the velocity profile because enhancement in incident radiations energizes the fluid flow, increasing the momentum boundary layer.

3.2. Fluid temperature results

Fig. 5 depicts the variation in fluid temperature results in boundary layer against numerous influential physical parameters. The plots 5(a) show the effect of Jeffrey fluid parameters (β_1 and β_2) on the temperature profile. This plot reveals that the temperature profile decelerates with enhancement in β_1. Noticeably, as β_1 increases, the temperature increases slightly towards the sheet surface. Therefore, the temperature increases close to the sheet's surface due to the fluid particle movements, which thicken the boundary layer of thermal profiles. Since the temperature differential in the free stream and the boundary layer is more significant at the sheet's surface, these motions increase fluid temperature near the surface of the sheet. Away from the surface of the sheet within the boundary layer, the temperature differential between the boundary layer and the free stream is minimal; as a result, the increased mobility of fluid particles does not affect the thickness of the boundary layer of the thermal profiles away from the surface of the sheet. Fig. 5(b) depicts dimensionless temperature curves for various β_2 values. The relaxation-to-retardation time ratio does not affect the fluid temperature, particularly near the sheet surface. When β_2 increases, the temperature rises away from the sheet, which has very little effects the temperature profiles near the surface of the sheet. Fig. 5(c) displays the effect of the modified Hartmann number on the temperature profile of the hybrid nanofluid flow, which declares that the increment in the modified Hartmann number enhances the fluid temperature. A higher modified Hartmann number produces stronger electromagnetic forces, strengthening the flow's boundary layer of thermal profiles, and hence the temperature profile improves with an increment in the modified Hartmann number. Fig. 5(d) represents the exponential index parameter's influence on the flow field's temperature profile. A higher exponential index parameter weakens the modified Hartmann number, diminishing the temperature profile. Fig. 5(e) illustrates the porosity parameter k_p behavior with the temperature profile. It has been observed that the temperature profile behaves ascendingly for increased values of the porosity parameter. It results from an increased thermal boundary layer caused by high porosity parameter values. The influence of the Forchheimer number F_r on the fluid temperature is outlined in Fig. 5(f). The aspect of the wall thickness parameter (α) on the fluid temperature is displayed in Fig. 5(g). With an increase in α, it is demonstrated that the thickness of boundary layer of thermal profiles decreases. In Fig. 5(h), the effects of power index parameter on the flow's thermal properties are picturized. When the value of the power index parameter rises, the fluid's temperature rises as well. When n increases, the thickness of the wall reduces, causing the surface to stretch more and speeding up the flow. The melting parameter Me impacts on the boundary layer's of the temperature distribution is depicted in Fig. 5(i). The Figure picturize that the increasing values of the melting heat parameter Me decline the temperature profile. Because enhancing the melting heat transfer absorbs more energy from the flow field, then the temperature profile diminishes. The conductive properties of the fluid are related to Nr. Physically, the fluid displays better conductive qualities at larger value of Nr. As a result, the fluid temperatures rise, as evidenced by the findings in Fig. 5(j), where the displayed temperature curves exhibit an upward trend as the radiation parameter's values rise because radiation causes a discharge of heat into the system in substantial amounts, raising the fluid's temperature. Figs. 5(k) and 5(l) reveal the influences of Cu and MWCNT nanoparticles concentration on the temperature profile, which clearly shows the higher concentration of the nanoparticles enhances the fluid temperature. This variation occurs due to thermal features of the Cu and MWCNT nanoparticles.

3.3. Engineering interest quantities

Drag coefficient (C_f),

$$C_f = \frac{\tau_s}{\rho(U_s)^2}, \quad \tau_s = \frac{\mu_{hnf}}{1+\lambda_1}\left[\frac{\partial u}{\partial y} + \lambda_2\left(u\frac{\partial^2 u}{\partial x\partial y} + v\frac{\partial^2 u}{\partial y^2}\right)\right]\Bigg|_{y=A(x+b)^{\frac{1-n}{2}}}, \tag{3.1}$$

Local Nusselt number microorganisms (Nu_x),

$$Nu_x = \frac{(x+b)q_s}{\kappa_{hnf}\left(T_s - T_l\right)}, \quad q_s = -\kappa_{hnf}\frac{\partial T}{\partial y}\Bigg|_{y=A(x+b)^{\frac{1-n}{2}}}. \tag{3.2}$$

Physical quantities in non-dimensionalized form by the use of similarity variables:

$$Re_x^{1/2}C_f = \sqrt{\frac{n+1}{2}}\frac{1}{1+\beta_1}\left[F''(\zeta) + \beta_2\left(\frac{3n-1}{2}F'(\zeta)F''(\zeta) - \frac{n+1}{2}F(\zeta)F'''(\zeta)\right)\right]\Bigg|_{\zeta=0},$$

$$Re_x^{-1/2}Nu_x = -\varepsilon_6\sqrt{\frac{n+1}{2}}\theta'(\zeta)\Bigg|_{\zeta=0}. \tag{3.3}$$
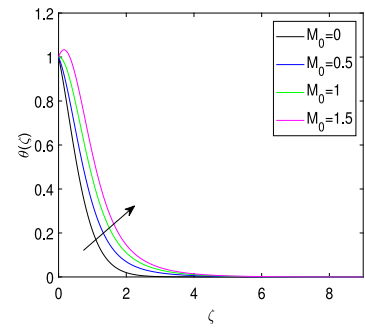
3.4. Drag coefficient results

The drag coefficient, i.e., volume flow rate results for numerous influential physical parameters, is depicted in Figs. 6(a)–6(b). In this Figure, plot 6(a) shows the impact of the Hartmann number and exponential index parameter on the drag coefficient, which reveals that the increment in exponential index enhances the drag coefficient and enhancement in Hartmann number decreases the
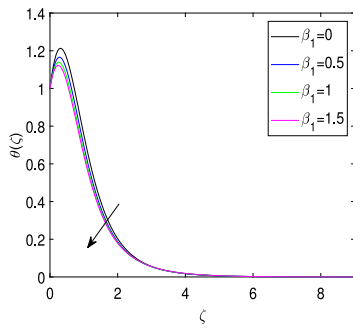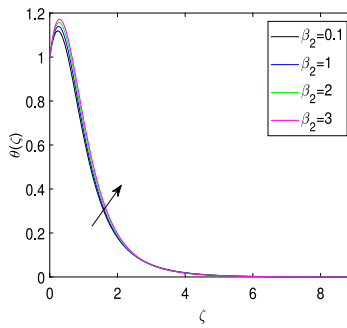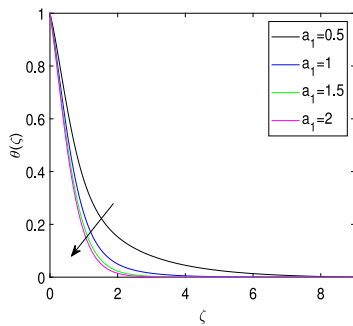
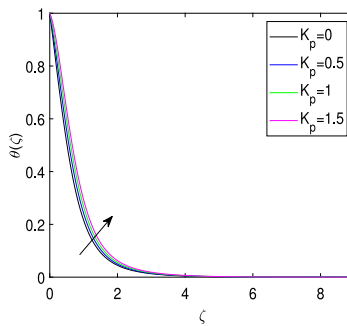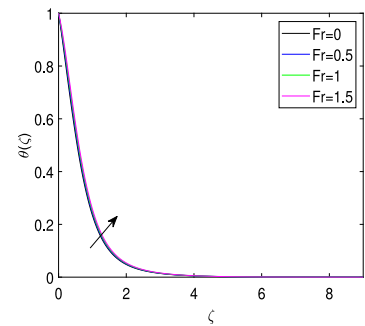(a) Variation in $\theta(\zeta)$ via β_1 (b) Variation in $\theta(\zeta)$ via β_2 (c) Variation in $\theta(\zeta)$ via M_0
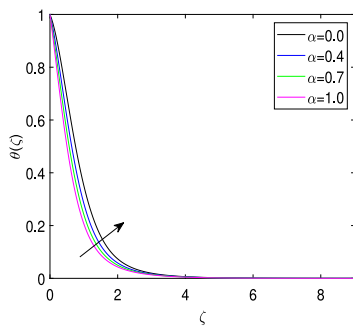
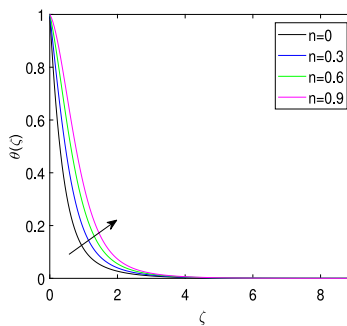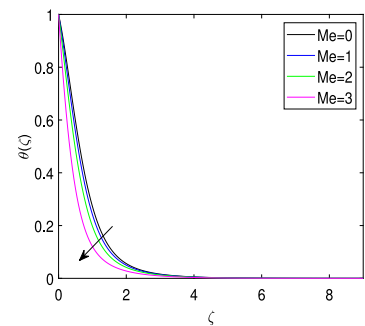(d) Variation in $\theta(\zeta)$ via a_1 (e) Variation in $\theta(\zeta)$ via k_p (f) Variation in $\theta(\zeta)$ via Fr
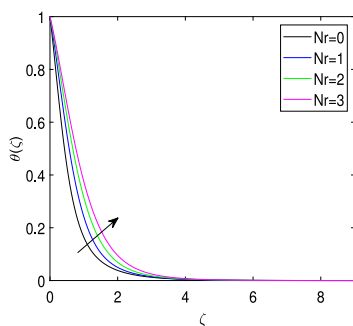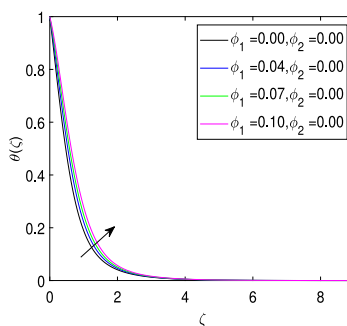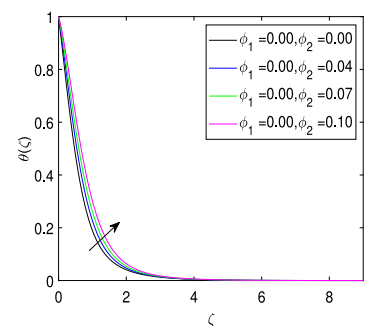
(g) Variation in $\theta(\zeta)$ via α (h) Variation in $\theta(\zeta)$ via n (i) Variation in $\theta(\zeta)$ via Me
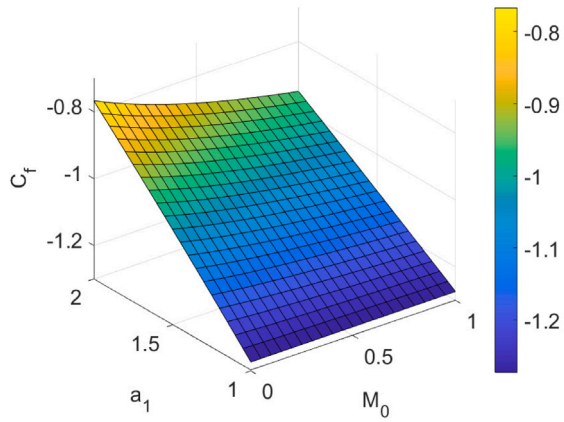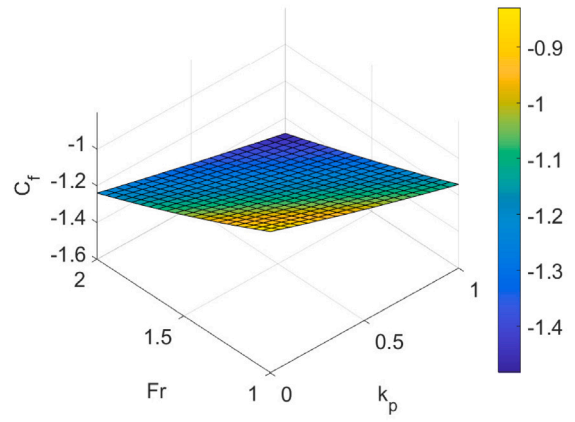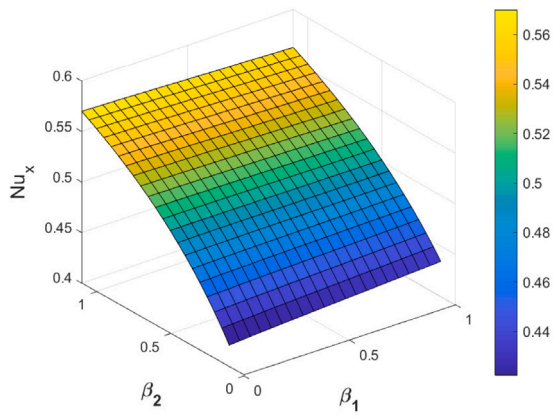
(j) Variation in $\theta(\zeta)$ via Nr (k) Variation in $\theta(\zeta)$ via ϕ_1 (l) Variation in $\theta(\zeta)$ via ϕ_2

Fig. 5. Plots of numerous influential physical parameters in terms of fluid temperature.

(a) Drag coefficient via M_0 and a_1

(b) Drag coefficient via Fr and K_p

(c) Nusselt number via β_1 and β_2
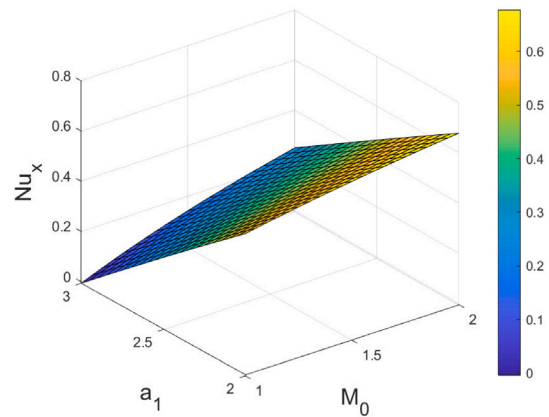
(d) Nusselt number via M_0 and a_1
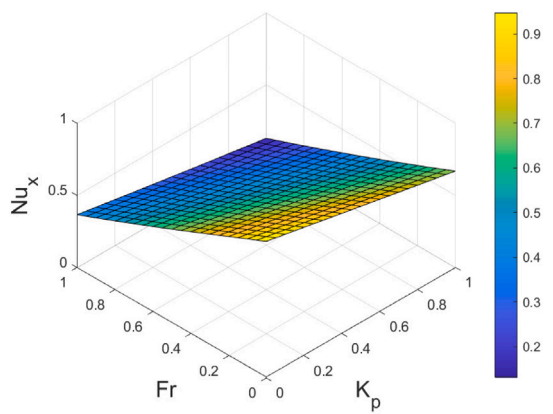
(e) Nusselt number via Fr and K_p
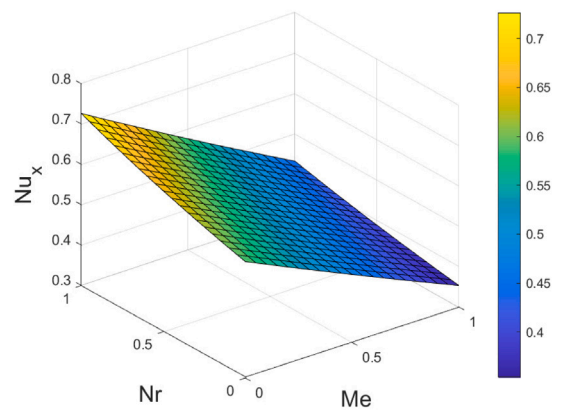
(f) Nusselt number via Nr and Me

Fig. 6. Plots of Nusselt number against various influencial physical parameter.

Table 3
Cases and scenarios.

Scenarios	Cases	β_1	β_2	Ha	a_1	Nr
1	1	0	0.5	0.5	0.5	0.5
	2	0.5	0.5	0.5	0.5	0.5
	3	1	0.5	0.5	0.5	0.5
2	1	0.5	1	0.5	0.5	0.5
	2	0.5	1.5	0.5	0.5	0.5
	3	0.5	1	2	0.5	0.5
3	1	0.5	1	0	0.5	0.5
	2	0.5	0.5	0.5	0.5	0.5
	3	0.5	0.5	1	0.5	0.5
4	1	0.5	0.5	0	1	0.5
	2	0.5	0.5	0.5	1.5	0.5
	3	0.5	0.5	0.5	2	0.5
5	1	0.5	0.5	1	0.5	0
	2	0.5	0.5	0.5	1	0.4
	3	0.5	0.5	0.5	1	0.8

Table 4
Artificial neural network outputs for all cases and scenarios.

Parameter	Case	Time	Mean square error			Performance	Gradient	Mu	Epoch
			Training	Validation	Testing				
β_1	1	16	2.2352e−12	8.8095e−08	8.5276e−09	2.24e−12	2.97e−07	1e−09	1000
	2	14	2.1551e−11	3.2657e−11	4.6390e−11	2.16e−11	1.27e−07	1e−08	1000
	3	12	1.5613e−12	7.5071e−12	9.1341e−12	1.56e−12	1e−07	1e−09	995
β_2	1	9	4.5641e−12	2.8992e−09	6.0355e−08	4.56e−12	9.98e−08	1e−09	726
	2	10	2.4393e−11	2.7780e−11	3.2996e−11	2.44e−11	1.36e−07	1e−08	1000
	3	11	3.8384e−10	6.0962e−09	7.8118e−10	3.84e−10	4.52e−07	1e−07	1000
M_0	1	4	9.7590e−13	1.5565e−12	1.1491e−12	9.76e−13	9.94e−08	1e−10	328
	2	8	3.2326e−12	2.7221e−11	7.1806e−11	3.23e−12	1e−07	1e−09	773
	3	8	3.3054e−12	1.2805e−11	6.1187e−12	3.31e−12	1e−07	1e−09	866
a_1	1	10	2.2513e−12	2.8180e−12	2.5807e−12	2.25e−12	1e−07	1e−09	952
	2	10	2.3543e−09	3.3378e−08	3.3701e−09	3.3701e−09	1.79e−06	1e−07	1000
	3	11	2.3713e−12	1.6375e−10	5.7232e−12	2.37e−12	9.98e−08	1e−09	999
Nr	1	9	2.9628e−11	4.2744e−11	2.4757e−09	2.96e−11	3.89e−07	1e−08	1000
	2	11	2.4710e−11	1.3572e−10	2.8648e−11	2.47e−11	1.16e−07	1e−08	1000
	3	10	4.2736e−11	1.8165e−07	8.4559e−09	4.27e−11	1.82e−07	1e−08	1000

drag coefficient. The plot 6(b) represent the variation in drag coefficient via the porosity parameter and Forchheimer number and declares that enhancement in the Forchheimer number and porosity parameter diminishes the drag coefficient.

3.5. Nusselt number results

Figs. 6(c)–6(f) illustrates the different results of the Nusselt number, i.e., heat transfer rate against numerous influential physical parameters. The Fig. 6(c) depicts the behavior of the Nusselt number via Jeffrey fluid parameters β_1 and β_2. As per this Figure, it is noted that the increase in Jeffrey fluid parameters β_1 and β_2 enhance the Nusselt number. But the effect of β_1 for magnifying heat transfer rate is negligibly minimal compared to β_2. The variation in Nusselt number via M_0 and a_1 is presented in Fig. 6(d). In this Figure, it is seen that the Nusselt number diminishes along escalating values of a_1 and improves along the escalating values of the M_0. Fig. 6(e) illustrates the influence of the Fr and K_p on the Nusselt number, which clears that enhancing values of both Fr and K_p decreases the Nusselt number. Fig. 6(f) examined the behavior of the Nusselt number against Nr and Me. This Figure reports that the growing values of Nr enhance the Nusselt number, and the increasing values of Me reduce the Nusselt number.

4. Modeling of artificial neural networking

Artificial neural networks have gained much attraction among contemporary researchers in recent years for their use in solving poorly defined or non-linear problems in various fields, including engineering, medicine, business, and cyber security. Its design comprises the nodes in hidden layers, network connections, initial weight modifications, and selection of activation functions. It is crucial for modeling ANNs, and its values typically rely on the nature of the problem. Training data is estimated from the numerical

work already defined in this study. The backpropagation algorithm is employed in this paper. Its distinctive feature is that the ANN modifies the weights' values and the target's biases in response to the gradient.

4.1. Levenberge Marquardt backpropagation (LMBP)

The Levenberg–Marquardt algorithm (LMA) is a well-known trust region approach used to find the minimum across a set of parameters of a (non-linear or linear) function. A trusted section of the objective function is modeled internally using a function such as quadratic. When a suitable match is identified, the trust region is increased. The Levenberg–Marquardt technique combines the neural network's gradient descent with the extremely powerful Gauss–Newton method for optimization. LMBP behaves like the Gauss–Newton method; nevertheless, it is guaranteed to converge the current results from the local minimum along the solution to have a more significant value.

4.2. Discussion of ANN results

Nusselt number is selected as the target or objective function for the input variable in the current communication. The proposed ANN-BLMS reference dataset results are calculated with a step size of 0.01 for input values ranging from 0 to 1, and 101 inputs are randomly distributed with 70% data for training and 15% for testing and validation. The programming continues until the desired output data is met by one of the stopping criteria. The training aims to reduce the sum of the mean square error function or to find a solution to the more appropriate problem as it approaches zero. Data of the different cases and scenarios are given in Table 3.

Artificial neural network outputs for the Nusselt number in the different terminologies related to the output data of the ANN and target values for case 1 in the first scenario are shown in Fig. 7. Plot 7(a) represents the validation performance graph in which the best performance of validation is 8.8095×10^{-08} occurs at 1000 epoch. The graph of function fit is plotted in Fig. 7(b), which declares the validation of convergence of ANN outputs, test targets, training targets, and training outputs. The training state plot of the ANN model is depicted in Fig. 7(c). These plots give essential information about convergence frequency and optimal epoch state. ANN models use mean square error for the convergence of optimal solution, which is the mean of squared values predicted by ANN and target values. For each of the model's epochs, MSE has been predetermined. The model deems validation failed whenever an epoch's MSE value exceeds that threshold. Six validation failures are the model's default termination condition. But for this case, the ANN model reaches to optimal solution within three validation failures. The gradient is the backpropagation gradient's logarithmic value for each iteration. It shows that the model has, at its lowest point, reached the local minimum of the objective function. The gradient value, in this case, is 2.9667^{-07}. The mu control parameter of the neural network training process. The convergence of errors directly depends on the selection of mu. Mu for this case is 10^{-09} at 1000 epoch. Fig. 7(d) illustrates the error histogram of the ANN model. Testing training, and validation datasets each has 70% of the total data. Samples from each of these three datasets were taken. The model was applied to every sample to forecast the output, and the results of desired or actual values are then compared with sample. A large number of samples were acquired. Afterward, errors were computed for each sample. These inaccuracies were divided into 20 groups. These 20 bins and the number of samples that made up the mistakes were shown together. In Fig. 7(d) y-axis in this graph displays the sample numbers with an error in the bin while the X-axis represents the error bins. The regression plot is displayed in Fig. 7(e). Regression is used here to refer to linear regression. These plots are produced when all validation, training, and testing data are utilized to predict the trained ANN, and a comparison is then made between the observed and actual values. The linear relationship in the targets and outcomes will determine the model's performance. It uses the formula $output = R \times target + bias$. The model is performing well if R = 1. If R is equal to 0, the model is a complete failure. The artificial neural network model outputs for case 1 of the second scenario are shown in Fig. 8. The validation performance is sketched in Fig. 8(a), and the best performance of the validation of training is at MSE of 2.8992×10^{-09} in 726 epochs. The function fit for the training outputs, training validation outputs, targets outputs and test outputs of this case is seen in Fig. 8(b). Fig. 8(c) depicts the training state plots for validation failure, mu, and gradient in which two validation failure occurs or mu and gradient values are 10^{-9} and 9.978×10^{-8} at 726 epoch. Histogram error plot and regression plots are picturized in Figs. 8(d) and 8(e). Artificial neural network outputs for case 1 in the third scenario with different terminologies are picturized in Fig. 9. Fig. 9(a) gives the validation performance plot of the training. The best validation performance is 1.5565×10^{-12} at 328 epoch. The function-fit plot for the output element in terms of test targets, training outputs, training targets, validation targets, test outputs, and errors is seen in Fig. 9(b). In training state plot, the training completed at 328 epoch with 9.9432×10^{-08} gradient and 10^{-10} mu in 1 validation failures as illustrated in Fig. 9(c). Error histogram and regression plots for training, validation, test, and error are plotted in Figs. 9(d) and 9(e). Artificial neural network outputs for case 1 in the fourth scenario are presented in Fig. 10. The validation performance result is illustrated in Fig. 10(a) in terms of validation and test, and this Figure reveals that the best performance of validation is 2.818×10^{-12} at 952 epoch. The fit function graph for the output elements in terms of test targets, training outputs, training targets, validation targets, test outputs, and errors is shown in Fig. 10(b). Plot for the training state is depicted in Fig. 10(c), which reveals that training stops in 952 epoch at 9.9972×10^{-08} gradient value and 10^{-09} mu value in no validation failures. Error histogram and regression plots for training, validation, and the test are displayed in Figs. 10(d) and 10(e). The mu, validation, training, performance, gradient, test, and epoch for all cases are shown in the Table 4. Overall it is concluded that ANN gives excellent convergent results with the lowest possible error.
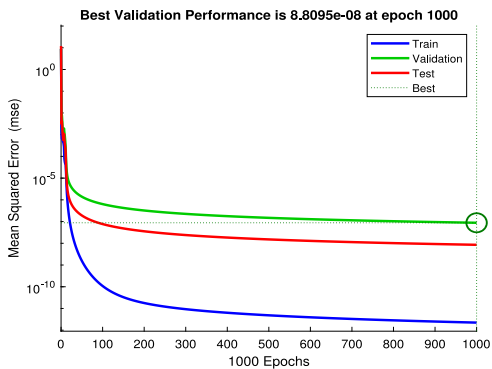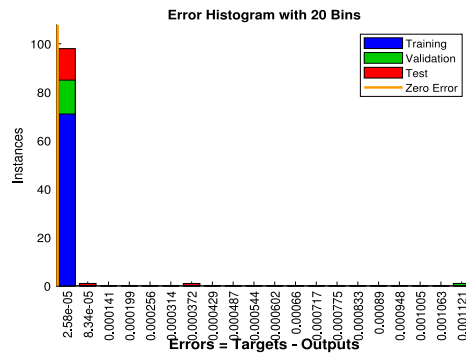
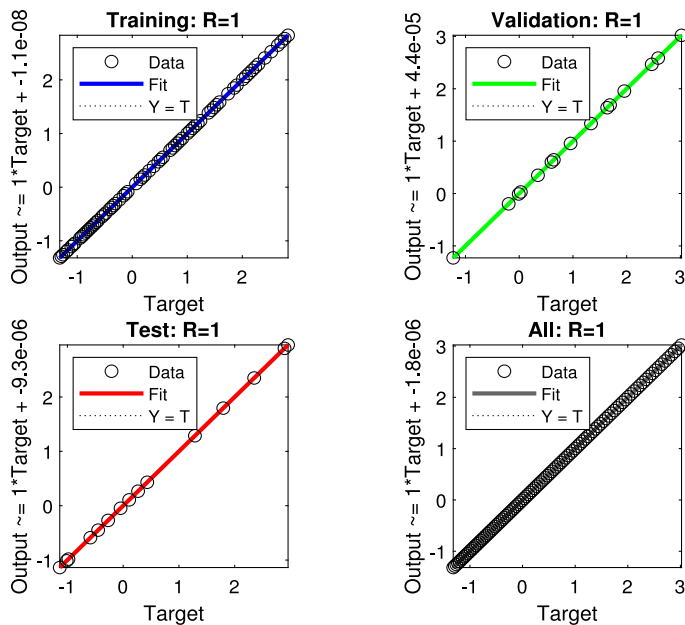(a) Validation performance plot
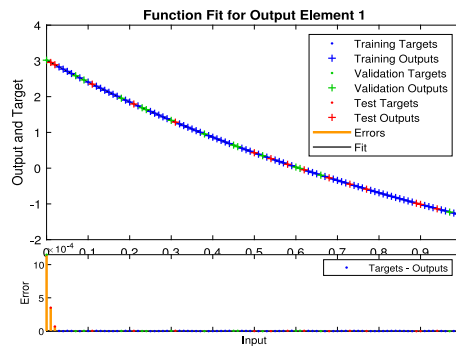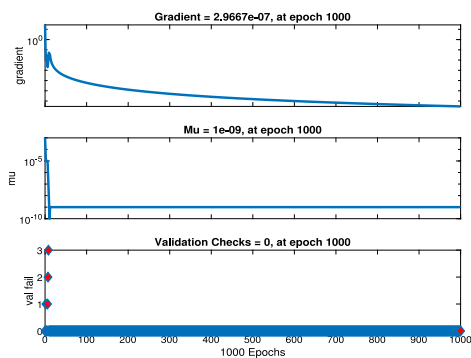
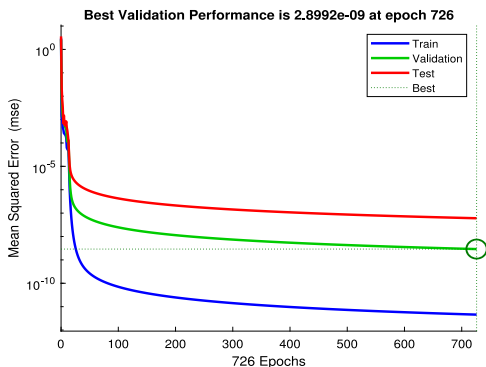(b) Function fit plot

(c) Training state plot
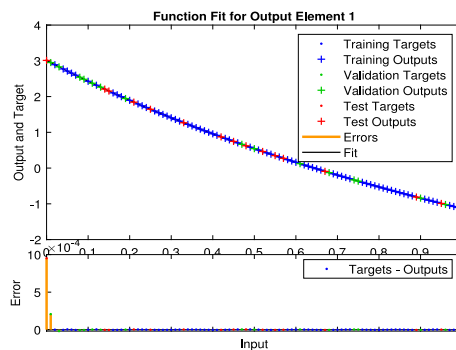

(d) Error histogram plot
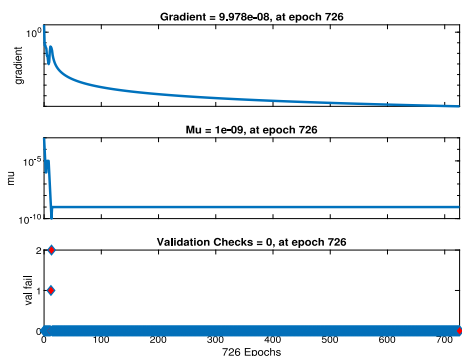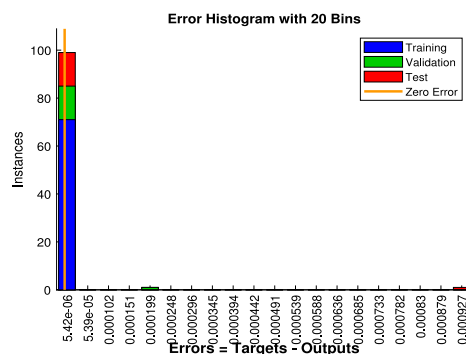

(e) Regression analysis plot

Fig. 7. ANN model outputs for case 1 in scenario 1.
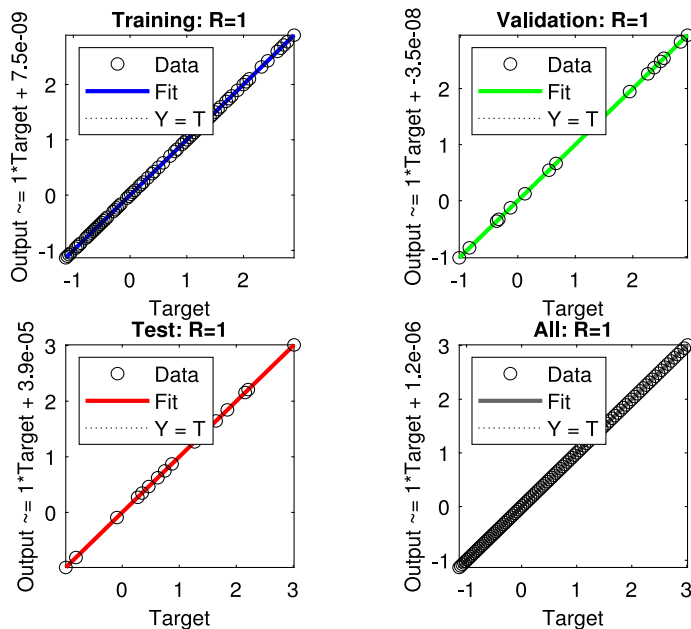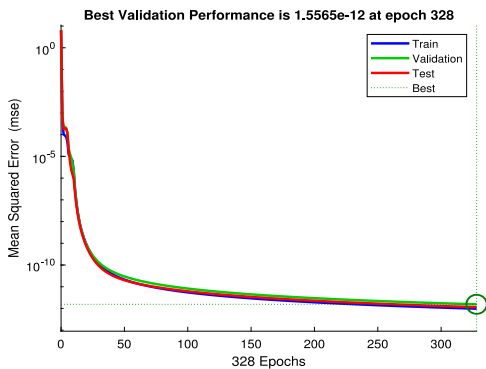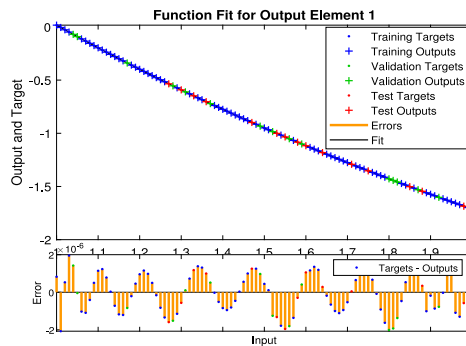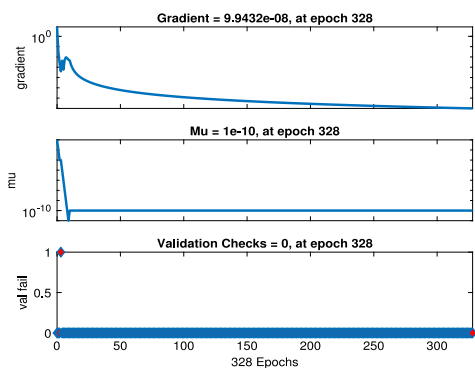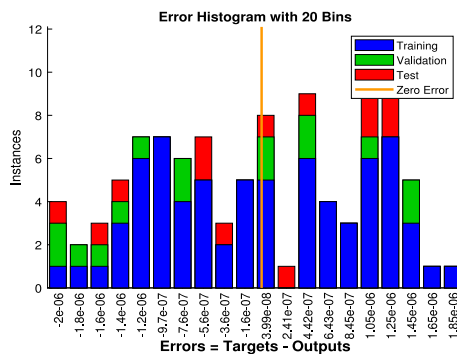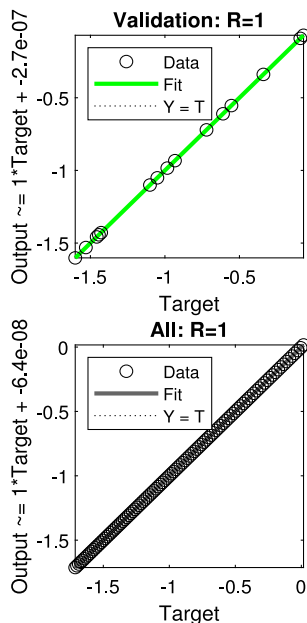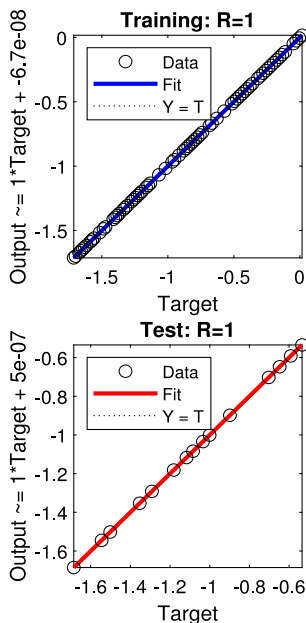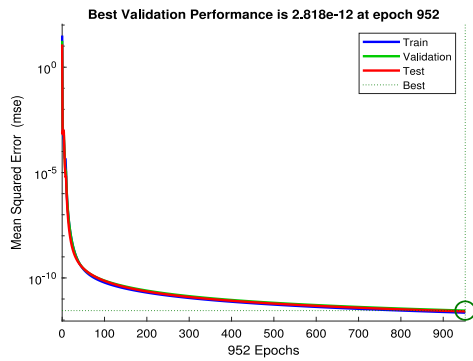
(a) Validation performance plot

(b) Function fit plot

(c) Training state plot

(d) Error histogram plot
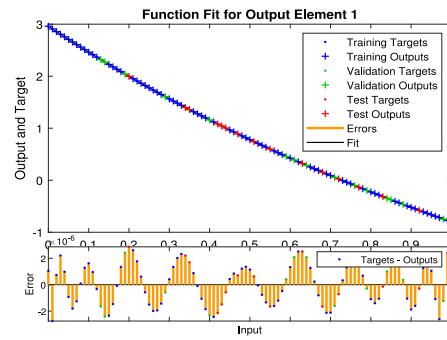

(e) Regression analysis plot

Fig. 8. ANN model outputs for case 1 in scenario 2.

(a) Validation performance plot

(b) Function fit plot

(c) Training state plot

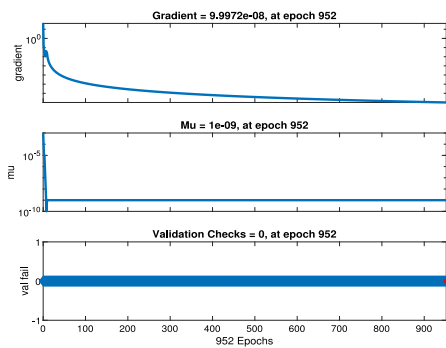(d) Error histogram plot

(e) Regression analysis plot

Fig. 9. ANN model outputs for case 1 in scenario 3.

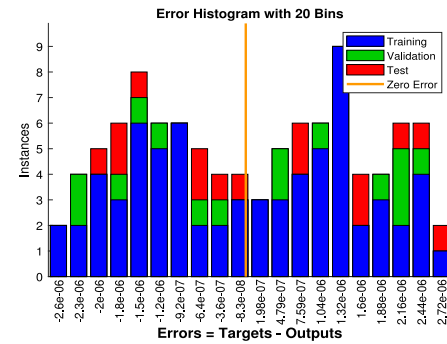(a) Validation performance plot
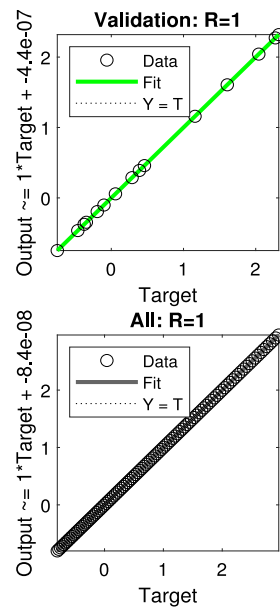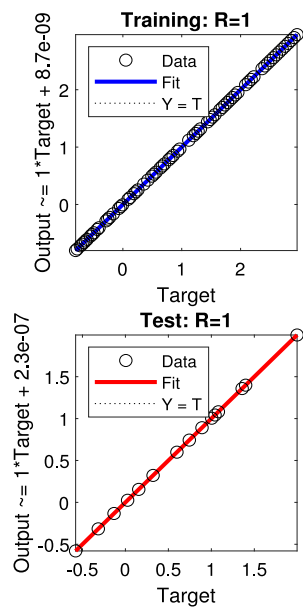

(b) Function fit plot

(c) Training state plot

(d) Error histogram plot

x y

(e) Regression analysis plot

Fig. 10. ANN model outputs for case 1 in scenario 4.

5. Conclusions

This study investigates the melting heat transfer in Jeffrey hybrid nanofluid flow for parabolic trough solar collectors due to solar radiation with the viscous dissipation, Ohmic heating, Darcy Forchheimer porous medium over variably thicked vertically elongating Riga surface. The governing equations are coupled higher-order PDEs which are than converted into ODEs by introducing appropriate similarity variables, and dimensionless numbers and parameters. The resulting higher order ODEs are than solved with Runga Kutta fourth-order numerical scheme in conjunction with shooting iterative technique. Major conclusions obtained from this study are:

- The velocity profile improves with increase in modified Hartmann number M_0 and reverse trend is obtained in case of escalating exponential index parameter a_1.
- Fluid velocity decelerates with an improvement in melting heat parameter Me, porosity parameter K_p, and Forchheimer number Fr while it increases with an enhancement in radiation parameter Nr
- The fluid thermal profiles accelerates with increase in Jeffrey fluid parameter β_2 and it decelerates with augmenting profile of Jeffrey fluid parameter β_1.
- The temperature profile rises for enhanced values of modified Hartmann number M_0 and worsens for enhanced values of exponential index parameter a_1.
- The wall thickness parameter α and melting heat parameter Me drops the thermal boundary layer, and power index parameter n and radiation parameter Nr improves the thermal boundary layer.
- Higher concentration of the nanoparticles also escalates the temperature profile.
- The escalating values of Jeffrey fluid parameters β_1 and β_2 enhances the Nusselt number i.e heat transfer rate.
- The Nusselt number diminishes along escalating values of exponential index parameter a_1 and improves along the escalating values of the modified Hartmann number M_0.
- The enhancing values of both Forchheimer number Fr and porosity parameter K_p decreases the Nusselt number Nu_x.
- Improvement in radiation parameter Nr enhances the Nusselt number and the growing values of melting heat parameter Me reduces the Nusselt number Nu_x.
- Artificial neural network is also used to determine the Nusselt number and it is concluded that the Artificial neural networking has a very good potential to work in this model to give the desired outputs with highest possible accuracy.

Radiant energy of the sun is a renewable energy source that is available in huge amounts in our living environment and has various applications in solar-powered appliances for cooking, air conditioning, solar-powered systems for treating wastewater, photovoltaic lighting, solar-powered cars, aircraft, etc. Parabolic trough solar collectors store the concentrated radiation energy to fulfill the requirement of high temperatures in thermal energy systems. The efficiency of PTSCs is improved by introducing hybrid nanoparticles in non-Newtonian fluid flows.

CRediT authorship contribution statement

Bhupendra K. Sharma: Project administration, Investigation, Resources, Writing & drafting. **Anup Kumar:** Conceptualization, Methodology, Software, Formal analysis, Writing – original draft. **Nidhish K. Mishra:** Formal analysis, Visualization, Validation. **Ibrahim Albaijan:** Methodology, Software, Formal analysis. **Unai Fernandez-Gamiz:** Software, Funding acquisition, Supervision.

Declaration of competing interest

The authors declare that they have no known competing financial interests or personal relationships that could have appeared to influence the work reported in this paper.

Data availability

No data was used for the research described in the article.

Acknowledgments

Appendix

Abbreviations	
ANN Artificial neural network	ODEs Ordinary differential equations
PDEs Partial differential equations	PTSCs Parabolic trough solar collectors

Nomenclature

a_1 Exponential index parameter	*Greek Letters*
C_f Drag coefficient	α Thickness parameter
C_p Capacity of heat at constant pressure	α_1 Thermal diffusivity
c_s Melting surface concentration	β_1 Relaxation time and retardation time ratio parameter
Ec Eckert number	β_2 Retardation time parameter
F' Fluid velocity in dimensionless form	$(\beta_T)_{hnf}$ Buoyancy force due to temperature
Fr Forchheimer number	κ Thermal conductivity
Gr Grashof number	λ_1 Relaxation time and retardation time ratio
k_p Porosity parameter	λ_2 Retardation time
n Power index of the stretching surface	μ_f Dynamic viscosity
Nr Radiation parameter	μ_{hnf} Hybrid nanofluid's dynamic viscosity
Nu_x Nusselt number	ν_{hnf} Hybrid nanofluid's kinematic viscosity
M_0 Hartmann number	ψ Stream function
Pr Prandtl number	ρ_{hnf} Density of fluid
T_l Ambient temperature	τ_s Shear stress
T_s Surface temperature	θ Fluid temperature in dimensionless form
U_s Elongating velocity of surface	ϕ_1 Concentration of Copper nanoparticles
u Fluid velocity along x-axis	ϕ_2 Concentration of multi-walled nanotubes
v Fluid velocity along y-axis	ζ Similarity variable

References

[1] L. Mu, Q. Zhu, L. Si, Radiative properties of nanofluids and performance of a direct solar absorber using nanofluids, in: International Conference on Micro/Nanoscale Heat Transfer, Vol. 43895, 2009, pp. 549–553.

[2] Q. Zhu, Y. Cui, L. Mu, L. Tang, Characterization of thermal radiative properties of nanofluids for selective absorption of solar radiation, Int. J. Thermophys. 34 (2013) 2307–2321.

[3] D. Rativa, L.A. Gómez-Malagón, Solar radiation absorption of nanofluids containing metallic nanoellipsoids, Sol. Energy 118 (2015) 419–425.

[4] S. Dugaria, M. Bortolato, D. Del Col, Modelling of a direct absorption solar receiver using carbon based nanofluids under concentrated solar radiation, Renew. Energy 128 (2018) 495–508.

[5] J. Subramani, P. Nagarajan, O. Mahian, R. Sathyamurthy, Efficiency and heat transfer improvements in a parabolic trough solar collector using TiO2 nanofluids under turbulent flow regime, Renew. Energy 119 (2018) 19–31.

[6] M. Malekan, A. Khosravi, S. Syri, Heat transfer modeling of a parabolic trough solar collector with working fluid of Fe_3O_4 and CuO/therminol 66 nanofluids under magnetic field, Appl. Therm. Eng. 163 (2019) 114435.

[7] S. Rostami, A. Shahsavar, G. Kefayati, A. Shahsavar Goldanlou, Energy and exergy analysis of using turbulator in a parabolic trough solar collector filled with mesoporous silica modified with copper nanoparticles hybrid nanofluid, Energies 13 (11) (2020) 2946.

[8] W. Jamshed, C. Şirin, F. Selimefendigil, M. Shamshuddin, Y. Altowairqi, M.R. Eid, Thermal characterization of coolant maxwell type nanofluid flowing in parabolic trough solar collector (PTSC) used inside solar powered ship application, Coatings 11 (12) (2021) 1552.

[9] W. Jamshed, K.S. Nisar, Computational single-phase comparative study of a Williamson nanofluid in a parabolic trough solar collector via the Keller box method, Int. J. Energy Res. 45 (7) (2021) 10696–10718.

[10] M. Arun, D. Barik, K. Sridhar, Experimental and CFD analysis of dimple tube parabolic trough solar collector (PTSC) with TiO2 nanofluids, J. Therm. Anal. Calorim. (2022) 1–18.

[11] W. Ajbar, J. Hernández, A. Parrales, L. Torres, Thermal efficiency improvement of parabolic trough solar collector using different kinds of hybrid nanofluids, Case Stud. Therm. Eng. (2023) 102759.

[12] K. Sopian, W.R.W. Daud, M.Y. Othman, B. Yatim, et al., Thermal performance of the double-pass solar collector with and without porous media, Renew. Energy 18 (4) (1999) 557–564.

[13] A.J. Chamkha, C. Issa, K. Khanafer, Natural convection from an inclined plate embedded in a variable porosity porous medium due to solar radiation, Int. J. Therm. Sci. 41 (1) (2002) 73–81.

[14] M. Gómez, D. Patiño, R. Comesaña, J. Porteiro, M.Á. Feijoo, J. Míguez, CFD simulation of a solar radiation absorber, Int. J. Heat Mass Transfer 57 (1) (2013) 231–240.

[15] B. Sharma, M. Sharma, R. Gaur, A. Mishra, Mathematical modeling of magneto pulsatile blood flow through a porous medium with a heat source, Int. J. Appl. Mech. Eng. 20 (2) (2015) 385–396.

[16] G. Ibáñez, A. López, J. Pantoja, J. Moreira, Entropy generation analysis of a nanofluid flow in MHD porous microchannel with hydrodynamic slip and thermal radiation, Int. J. Heat Mass Transfer 100 (2016) 89–97.

[17] T. Chakraborty, K. Das, P.K. Kundu, Ag-water nanofluid flow over an inclined porous plate embedded in a non-Darcy porous medium due to solar radiation, J. Mech. Sci. Technol. 31 (2017) 2443–2449.

[18] B. Tripathi, B. Sharma, Effect of heat transfer on MHD blood flow through an inclined stenosed porous artery with variable viscosity and heat source, Romanian J. Biophys. 28 (3) (2018) 89–102.

[19] B.K. Sharma, U. Khanduri, N.K. Mishra, A.J. Chamkha, Analysis of arrhenius activation energy on magnetohydrodynamic gyrotactic microorganism flow through porous medium over an inclined stretching sheet with thermophoresis and Brownian motion, Proc. Inst. Mech. Eng. E (2022) 09544089221128768.

[20] C. Kumawat, B. Sharma, Q.M. Al-Mdallal, M. Rahimi-Gorji, Entropy generation for MHD two phase blood flow through a curved permeable artery having variable viscosity with heat and mass transfer, Int. Commun. Heat Mass Transfer 133 (2022) 105954.

[21] B. Sharma, R. Gandhi, Combined effects of joule heating and non-uniform heat source/sink on unsteady MHD mixed convective flow over a vertical stretching surface embedded in a Darcy-Forchheimer porous medium, Propuls. Power Res. 11 (2) (2022) 276–292.

[22] A. Pantokratoras, E. Magyari, EMHD free-convection boundary-layer flow from a riga-plate, J. Eng. Math. 64 (2009) 303–315.

[23] M. Farooq, A. Anjum, T. Hayat, A. Alsaedi, Melting heat transfer in the flow over a variable thicked riga plate with homogeneous-heterogeneous reactions, J. Mol. Liquids 224 (2016) 1341–1347.

[24] A. Anjum, N. Mir, M. Farooq, M.I. Khan, T. Hayat, Influence of thermal stratification and slip conditions on stagnation point flow towards variable thicked riga plate, Results Phys. 9 (2018) 1021–1030.

[25] P. Ragupathi, A.A. Hakeem, Q.M. Al-Mdallal, B. Ganga, S. Saranya, Non-uniform heat source/sink effects on the three-dimensional flow of Fe3O4/Al2O3 nanoparticles with different base fluids past a riga plate, Case Stud. Therm. Eng. 15 (2019) 100521.

[26] K. Hosseinzadeh, A. Asadi, A. Mogharrebi, J. Khalesi, S. Mousavisani, D. Ganji, Entropy generation analysis of (CH2oh) 2 containing CNTs nanofluid flow under effect of MHD and thermal radiation, Case Stud. Therm. Eng. 14 (2019) 100482.

[27] A. Zaib, U. Khan, I. Khan, A. H. Seikh, E.-S. M. Sherif, Entropy generation and dual solutions in mixed convection stagnation point flow of micropolar Ti6Al4V nanoparticle along a riga surface, Processes 8 (1) (2019) 14.

[28] M. Shoaib, M.A.Z. Raja, M.A.R. Khan, I. Farhat, S.E. Awan, Neuro-computing networks for entropy generation under the influence of MHD and thermal radiation, Surf. Interfaces 25 (2021) 101243.

[29] B. Sharma, A. Kumar, R. Gandhi, M. Bhatti, Exponential space and thermal-dependent heat source effects on electro-magneto-hydrodynamic Jeffrey fluid flow over a vertical stretching surface, Internat. J. Modern Phys. B 36 (30) (2022) 2250220.

[30] S. Salawu, A. Obalalu, S. Okoya, Thermal convection and solar radiation of electromagnetic actuator Cu–Al2O3/C3H8O2 and Cu–C3H8O2 hybrid nanofluids for solar collector optimization, Mater. Today Commun. 33 (2022) 104763.

[31] B. Sharma, R. Gandhi, N.K. Mishra, Q.M. Al-Mdallal, Entropy generation minimization of higher-order endothermic/exothermic chemical reaction with activation energy on MHD mixed convective flow over a stretching surface, Sci. Rep. 12 (1) (2022) 17688.

[32] R. Gandhi, B.K. Sharma, N.K. Mishra, Q.M. Al-Mdallal, Computer simulations of EMHD casson nanofluid flow of blood through an irregular stenotic permeable artery: Application of Koo-Kleinstreuer-Li correlations, Nanomaterials 13 (4) (2023) 652.

[33] B.K. Sharma, A. Kumar, R. Gandhi, M.M. Bhatti, N.K. Mishra, Entropy generation and thermal radiation analysis of EMHD jeffrey nanofluid flow: Applications in solar energy, Nanomaterials 13 (3) (2023) 544.

[34] S. Sharma, A. Dadheech, A. Parmar, J. Arora, Q. Al-Mdallal, S. Saranya, MHD micro polar fluid flow over a stretching surface with melting and slip effect, Sci. Rep. 13 (1) (2023) 10715.

[35] N. Abbas, S. Nadeem, M. Malik, Theoretical study of micropolar hybrid nanofluid over riga channel with slip conditions, Physica A 551 (2020) 124083.

[36] P. Sudarsana Reddy, P. Sreedevi, Entropy generation and heat transfer analysis of magnetic hybrid nanofluid inside a square cavity with thermal radiation, Eur. Phys. J. Plus 136 (1) (2021) 1–33.

[37] A.K. Tiwari, V. Kumar, Z. Said, H. Paliwal, A review on the application of hybrid nanofluids for parabolic trough collector: Recent progress and outlook, J. Clean. Prod. 292 (2021) 126031.

[38] F.S. Bayones, W. Jamshed, S. Elhag, M. Rabea Eid, Computational Galerkin finite element method for thermal hydrogen energy utilization of first grade viscoelastic hybrid nanofluid flowing inside PTSC in solar powered ship applications, Energy Environ. (2022) 0958305X221081463.

[39] B. Sharma, R. Gandhi, M. Bhatti, Entropy analysis of thermally radiating MHD slip flow of hybrid nanoparticles (Au-Al2O3/Blood) through a tapered multi-stenosed artery, Chem. Phys. Lett. 790 (2022) 139348.

[40] S. Saranya, L. Baranyi, Q.M. Al-Mdallal, Free convection flow of hybrid ferrofluid past a heated spinning cone, Therm. Sci. Eng. Prog. 32 (2022) 101335.

[41] R. Gandhi, B.K. Sharma, O.D. Makinde, Entropy analysis for MHD blood flow of hybrid nanoparticles (au–al2o3/blood) of different shapes through an irregular stenosed permeable walled artery under periodic body acceleration: Hemodynamical applications, ZAMM-J. Appl. Math. Mech./Z. Angew. Math. Mech. (2022) e202100532.

[42] N.S. Khashi'ie, I. Waini, N.M. Arifin, I. Pop, Dual solutions of unsteady two-dimensional electro-magneto-hydrodynamics (EMHD) axisymmetric stagnation-point flow of a hybrid nanofluid past a radially stretching/shrinking riga surface with radiation effect, Internat. J. Numer. Methods Heat Fluid Flow 33 (1) (2023) 333–350.

[43] Y. Salah, O. Al Mukbel, Y. Sabsabi, S. Saranya, Q.M. Al-Mdallal, F. Mukhamedova, Influence of PST and PHF heating conditions on the swirl flow of Al+ Mg+ TiO2 ternary hybrid water-ethylene glycol based nanofluid with a rotating cone, Int. J. Thermofluids 19 (2023) 100371.

[44] S. Saranya, F.Z. Duraihem, A.L. Isaac Lare, Q.M. Al-Mdallal, Quartic autocatalysis on horizontal surfaces with an asymmetric concentration: water-based ternary-hybrid nanofluid carrying titania, copper, and alumina nanoparticles, Phys. Scr. (2023).

[45] F. Shahzad, W. Jamshed, K.S. Nisar, M.M. Khashan, A.-H. Abdel-Aty, Computational analysis of ohmic and viscous dissipation effects on MHD heat transfer flow of Cu-PVA jeffrey nanofluid through a stretchable surface, Case Stud. Therm. Eng. 26 (2021) 101148.

[46] A. Kumar, B.K. Sharma, R. Gandhi, N.K. Mishra, M. Bhatti, Response surface optimization for the electromagnetohydrodynamic Cu-polyvinyl alcohol/water jeffrey nanofluid flow with an exponential heat source, J. Magn. Magn. Mater. 576 (2023) 170751.

[47] N.A. Zainal, R. Nazar, K. Naganthran, I. Pop, The impact of thermal radiation on Maxwell hybrid nanofluids in the stagnation region, Nanomaterials 12 (7) (2022) 1109.

[48] A. Wakif, A. Chamkha, I. Animasaun, M. Zaydan, H. Waqas, R. Sehaqui, Novel physical insights into the thermodynamic irreversibilities within dissipative EMHD fluid flows past over a moving horizontal riga plate in the coexistence of wall suction and joule heating effects: a comprehensive numerical investigation, Arab. J. Sci. Eng. 45 (2020) 9423–9438.